

**Antimony(+5) Ion Induced Tunable Intramolecular Charge  
Transfer in Hypervalent Antimony(V) Porphyrins**

Journal:	<i>Dalton Transactions</i>
Manuscript ID	DT-ART-03-2022-000675.R2
Article Type:	Paper
Date Submitted by the Author:	19-Mar-2022
Complete List of Authors:	Holzer, Noah; University of Minnesota Duluth Sharma, Jatan K.; University of North Texas Peterson, Steven; University of Minnesota Duluth Bayard, Brandon; University of Minnesota Duluth Nesterov, Vladimir; University of North Texas Karr, Paul; Wayne State College D'Souza, Francis; University of North Texas Poddutoori, Prashanth; University of Minnesota Duluth

## ARTICLE

## Antimony(+5) Ion Induced Tunable Intramolecular Charge Transfer in Hypervalent Antimony(V) Porphyrins†

Received 00th January 20xx,  
Accepted 00th January 20xx

Noah Holzer,<sup>a,||</sup> Jatan K. Sharma,<sup>b,||</sup> Steven Peterson,<sup>a</sup> Brandon J. Bayard,<sup>a</sup> Vladimir N. Nesterov,<sup>b</sup> Paul A. Karr,<sup>c</sup> Francis D'Souza,<sup>b,\*</sup> Prashanth K. Poddutoori<sup>a,\*</sup>

DOI: 10.1039/x0xx00000x

The +5 oxidation state of antimony induces push-pull style intramolecular charge transfer in an elegantly designed axial dimethoxyantimony(V) porphyrin series: SbP(OMe)<sub>2</sub>.PF<sub>6</sub>, SbMP(OMe)<sub>2</sub>.PF<sub>6</sub>, SbDMP(OMe)<sub>2</sub>.PF<sub>6</sub>, SbTMP(OMe)<sub>2</sub>.PF<sub>6</sub> with phenyl (P), 4-methoxyphenyl (MP), 3, 5-dimethoxyphenyl (DMP), and 3,4,5-trimethoxyphenyl (TMP) units, respectively, in its meso positions. The Sb(+5) makes the porphyrin ring electron-poor, whereas the methoxy groups on the phenyl unit produced electron-rich sites within the molecule. The presence of electron-poor and electron-rich parts in the same molecule resulted in a push-pull type intramolecular charge transfer (ICT). However, the ICT is strongly dependent on the position of the methoxy groups on the phenyl ring. The charge transfer character is more pronounced in *meta*-methoxy substituted antimony(V) derivatives (SbDMP(OMe)<sub>2</sub>.PF<sub>6</sub>, SbTMP(OMe)<sub>2</sub>.PF<sub>6</sub>) than the *para*-methoxy or no-methoxy substituted antimony(V) derivatives (SbP(OMe)<sub>2</sub>.PF<sub>6</sub>, SbMP(OMe)<sub>2</sub>.PF<sub>6</sub>). Steady-state and transient spectroscopic techniques, as well as solvatochromism techniques, were employed to establish the tunable ICT. Additionally, time-dependant density functional theory (TD-DFT) calculations were used to complement the experimental results. The systematic study of antimony(V) porphyrins, especially tunable push-pull nature could play an important role in instigating high yield charge-separated states in multi-modular donor-acceptor systems for solar energy conversion and molecular electronic and photonic applications.

### Introduction

Donor-acceptor (D-A) systems with “push-pull” architecture have gained a lot of attention in recent years because of their impressive properties towards a variety of applications.<sup>1–4</sup> For instance, a porphyrin comprised of a push-pull system with an electron-donating group at the peripheral position and an electron-withdrawing group at the opposite led to remarkably improved solar energy conversion efficiencies in dye-sensitized solar cells.<sup>5–10</sup> This nature not only minimizes the energy-wasting electron recombination in electron transfer reactions but also provides directionality to electron flow thus increasing the efficiencies of the photoinduced processes. Additionally, these systems showed potential applications in mimicking photosynthetic components,<sup>2,11–13</sup> molecular electronics and photonics,<sup>14</sup> and nonlinear optics.<sup>15,16</sup> Within these D-A systems, porphyrin molecules evolved as ideal photosensitizers due to their versatile optical, redox, and structural properties.

To introduce the push-pull nature in porphyrin, several synthetically challenging strategies were employed. The most common one has been linking (or fusing) the electron-rich and electron-poor units on the peripheral positions, either meso- or  $\beta$ -pyrrolic, of the porphyrin ring.<sup>3,10,13</sup>

Despite impressive design strategies, it has never been attempted to utilize the central element in the porphyrin cavity to induce the push-pull behaviour. Among porphyrin molecules, the main group porphyrins hold unique redox and structural properties. By insertion of a specific main-group element in the porphyrin cavity, it is feasible to tune the porphyrin properties for a specific role, that is either as electron donor or electron acceptor, in D-A systems. For example, insertion of aluminium(III) ion makes the porphyrin predominantly an electron donor,<sup>17</sup> whereas phosphorus(V) ion insertion makes the porphyrin an electron acceptor.<sup>18–20</sup> In addition, both the aluminium(III) porphyrin and phosphorus(V) porphyrin have similar axial bonding capabilities. Making use of these advantages, recently, we reported a push-pull type  $\mu$ -oxo porphyrin heterodimer which exhibits intramolecular charge transfer (ICT) from aluminium(III) porphyrin to phosphorus(V) porphyrin.<sup>21</sup>

Within the main-group, group 15 porphyrins, such as phosphorus(V) and antimony(V) porphyrins, have distinctive properties. Both porphyrins hold relatively high oxidation potentials compared to other main-group or transition metal

<sup>a</sup> Department of Chemistry & Biochemistry, University of Minnesota Duluth, 1039 University Drive, Duluth, Minnesota 55812, USA. Email: ppk@d.umn.edu

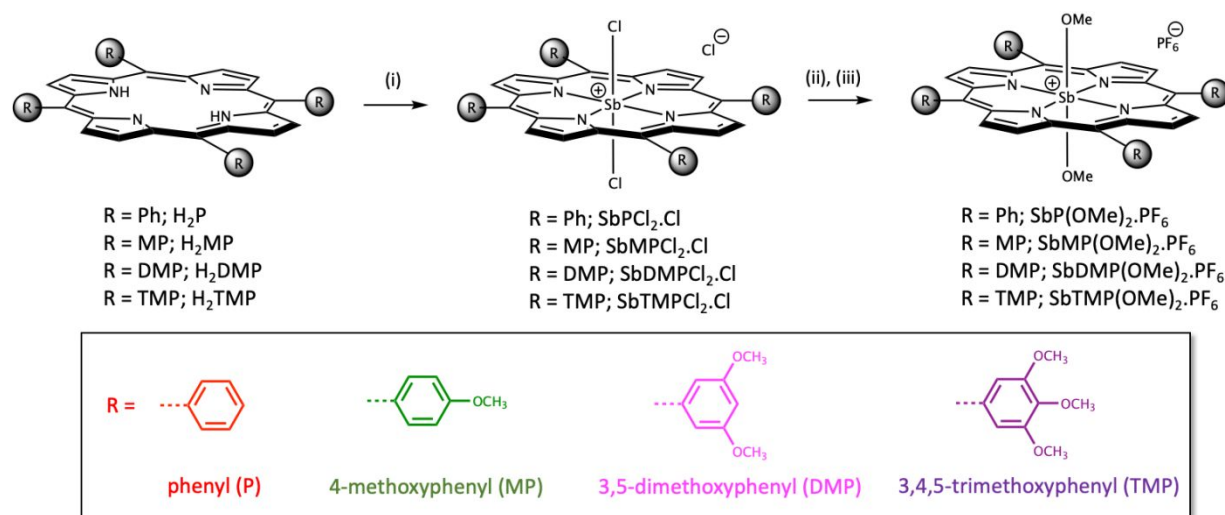
<sup>b</sup> Department of Chemistry, University of North Texas, 1155 Union Circle, # 305070, Denton, Texas 76203-5017, USA. Email: francis.dsouza@unt.edu

<sup>c</sup> Department of Physical Sciences and Mathematics, Wayne State College, 1111 Main Street, Wayne, Nebraska 68787, USA.

†Electronic Supplementary Information (ESI) available: Crystallography data, details of synthesis and physical methods, ESI mass spectra, NMR spectra, absorption spectra and data, Beer-Lambert curves, electrochemical voltammograms, fluorescence spectra, phosphorescence spectra, and transient absorption spectra. See DOI: 10.1039/x0xx00000x

||Equal contribution.

## ARTICLE



**Scheme 1.** Synthesis and nomenclature of the investigated antimony(V) porphyrins. Reaction conditions: (i)  $\text{SbCl}_5$ , Pyridine (ii)  $\text{CH}_3\text{OH}$ ,  $\text{CHCl}_3$ , Pyridine, and (iii)  $\text{NH}_4\text{PF}_6$

porphyrins.<sup>18,20,22–25</sup> Therefore, in principle, it is possible to induce the push-pull charge transfer in porphyrin molecules by utilizing the high oxidation state of antimony and phosphorus ions. To test this hypothesis, Sb(+5) ion was inserted in a series of tetraarylporphyrins, where the meso-aryl (= phenyl(P), 4-methoxyphenyl (MP), 3,5-dimethoxyphenyl (DMP), and 3,4,5-trimethoxyphenyl(TMP)) group is systematically changed to evaluate its role. The structures of these compounds are shown in Scheme 1. The high-valent antimony(V) centre is known to withdraw electron density from the porphyrin ring. As predicted, a strong intramolecular charge transfer (ICT) was observed in the molecule. This is because the Sb(+5) insertion creates both electron-rich and electron-deficient parts within the porphyrin structure. This method shows an alternative way to create a push-pull style ICT without opting synthetically challenging strategies. Using steady-state and transient spectroscopic techniques, accompanied by computational methods, the study unravels the intricate factors which induce the push-pull type charge transfer property as a function of meso-substitutions. Remarkably, the ICT can be turned on and off by selecting the methoxy positions on the aryl group.

The rich redox chemistry of the photoexcited antimony(V) porphyrins have been studied towards photocatalysis and electrocatalysis applications,<sup>23,26–28</sup> donor-acceptor systems,<sup>22,23,29,30</sup> and artificial photosynthetic applications.<sup>23,31</sup> The axial-bonding minimizes aggregation effects of the porphyrins allowing for increased optical properties and providing an optimal surface for use in photochemical reactions.<sup>32–35</sup> Combining the high oxidizing property of antimony(V) porphyrins and push-pull style ICT along with their

robust axial bonding capabilities provides tremendous opportunity for the use of these photosensitizers in the design of supramolecular architectures for artificial photosynthesis, optoelectronics, dye-sensitized photovoltaics, and photocatalysis applications.

## Results and discussion

### Synthesis

Scheme 1 summarizes the reaction that was used to obtain the target molecules. Free-base and antimony(V) porphyrins were prepared by previously established methods.<sup>25,36,37</sup> However, necessary modifications were adopted to suit the present set of porphyrins. The antimony(V) insertion in all the free-base porphyrins was achieved within 1 h by using  $\text{SbCl}_5$  to get the dichloroantimony(V) porphyrins. Column chromatography was utilized extensively to purify dichloroantimony(V) porphyrins. Additionally, a counterion exchange technique was also used for  $\text{SbP}(\text{Cl})_2$  and  $\text{SbDMP}(\text{Cl})_2$  to remove additional impurities. At this stage, the antimony(V) porphyrins possess two active axial Sb—Cl bonds. These bonds were utilized to react with methanol to synthesize the target axial dimethoxyantimony(V) porphyrins. Interestingly, the reaction times with methanol strongly depend on the position and number of the methoxy substitutions. The reactivity of dichloroantimony(V) porphyrins follows:  $\text{SbP}(\text{Cl})_2^+$  (1 h) >  $\text{SbDMP}(\text{Cl})_2^+$  (21 h) >  $\text{SbMP}(\text{Cl})_2^+$  (48 h) >  $\text{SbTMP}(\text{Cl})_2^+$  (72 h). This trend suggests that the reactivity of Sb—Cl bond directly depends on the electron density of the porphyrin ring, i.e. the

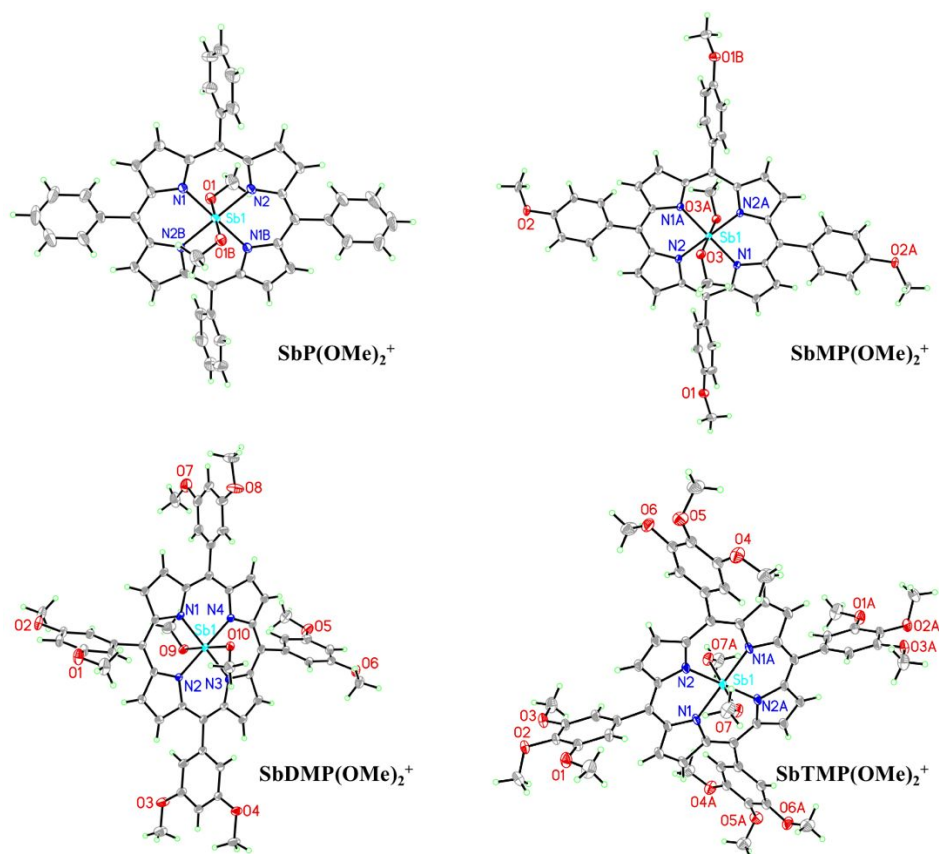


**Figure 1.** X-ray crystal structures of the investigated antimony(V) porphyrins with 30% ellipsoids. For clarity, the counterion  $\text{PF}_6^-$  and the co-crystallized solvent molecules are omitted.

increase in the electron density reduces the Sb—Cl reactivity. As the *p*-substituted groups are better electron directing than the *m*-substituted groups to increase the electron density on the ring (discussed in below sections), therefore, it is reasonable to witness a longer reaction time for  $\text{SbTMPCl}_2^+$  than the  $\text{SbMPCl}_2^+$  and  $\text{SbDMPCl}_2^+$ . The  $\text{SbP}_2^+$  do not possess any methoxy substitution, therefore, it is the most reactive porphyrin in the studied series.

### Structural characterization

Single crystals of the studied porphyrins suitable for X-ray diffraction studies were grown via the slow diffusion method, see the experimental section for details. The compounds crystallize with  $\text{PF}_6^-$  counterion and solvent molecules in the asymmetric unit. The molecular structures of the investigated porphyrins are presented in Figure 1 and the bond length, bond angles, and dihedral angles are summarized in Tables S1–S13. Additional crystallographic data for these compounds can be obtained from the Cambridge Crystallographic Data Centre (2130977, 2130978, 2130979, and 2130980 for  $\text{SbP}(\text{OMe})_2^+$ ,  $\text{SbMP}(\text{OMe})_2^+$ ,  $\text{SbDMP}(\text{OMe})_2^+$  and  $\text{SbTMP}(\text{OMe})_2^+$ , respectively). Detailed analysis of the coordinates reveals that the meso-substituted aryl units are tilted with respect to the porphyrin macrocycle such that the dihedral angle is between  $61.50 - 71.49^\circ$ ,  $64.14 - 66.56^\circ$ ,  $64.41 - 87.34^\circ$ , and  $58.40 - 77.98^\circ$  for  $\text{SbP}(\text{OMe})_2^+$ ,  $\text{SbMP}(\text{OMe})_2^+$ ,  $\text{SbDMP}(\text{OMe})_2^+$  and

$\text{SbTMP}(\text{OMe})_2^+$ , respectively. The antimony atom lies essentially within the plane of the 4 nitrogens of the porphyrin ring.

Preliminary characterization of the investigated compounds was carried out by ESI mass spectrometry and the data is spectra are shown in Figures S1–S4. As shown, the mass spectrum of each antimony(V) porphyrin showed an intense peak which corresponds to the mass ( $m/z$ ) of  $[\text{M} - \text{PF}_6]^+$ . The  $^1\text{H}$ ,  $^{13}\text{C}$ ,  $^{31}\text{P}$  and  $^{19}\text{F}$  NMR spectra of antimony(V) porphyrin are shown in Figures S5–S8. Shielding effects are apparent for the protons on the axial methoxy unit. The methoxy protons are strongly shifted upfield to  $\sim -2.00$  ppm in the antimony(V) porphyrin due to the ring current effect of the porphyrin macrocycle. The  $^{31}\text{P}$  NMR spectra of all the investigated compounds also revealed a septet between  $-144.53$  to  $-145.29$  ppm from the  $\text{PF}_6^-$  counterion.

### Absorption studies

The UV–visible spectra of antimony(V) porphyrins ( $\text{SbP}(\text{OMe})_2\cdot\text{PF}_6$ ,  $\text{SbMP}(\text{OMe})_2\cdot\text{PF}_6$ ,  $\text{SbDMP}(\text{OMe})_2\cdot\text{PF}_6$  and  $\text{SbTMP}(\text{OMe})_2\cdot\text{PF}_6$ ) and their free-base porphyrins ( $\text{H}_2\text{P}$ ,  $\text{H}_2\text{MP}$ ,  $\text{H}_2\text{DMP}$ , and  $\text{H}_2\text{TMP}$ ) are measured in  $\text{CH}_3\text{CN}$ ,  $\text{CH}_2\text{Cl}_2$ , and toluene. The spectra of antimony(V) porphyrins and free-base porphyrins are shown in Figure 2 and Figure S9 in  $\text{CH}_2\text{Cl}_2$ , respectively, and the data are summarized in Tables 1 and S14. As shown in Figure S9, each free-base porphyrin exhibited a typical  $\text{D}_{2h}$  symmetry type porphyrin spectrum with a B-band

## Article

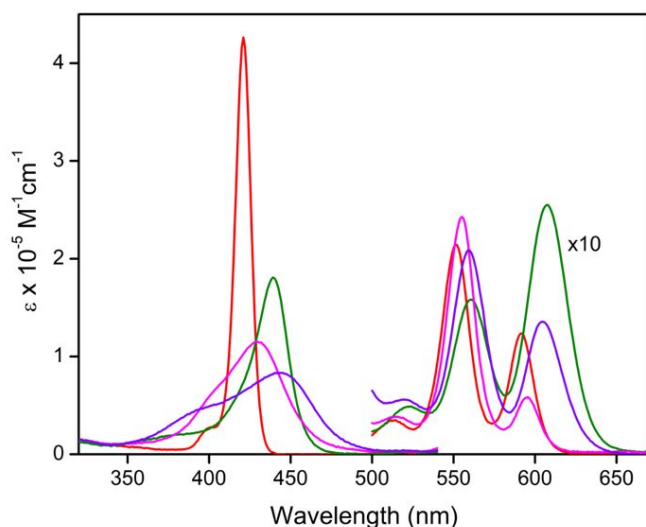


**Figure 2.** (a) UV-visible absorption spectra of SbP(OMe)<sub>2</sub>.PF<sub>6</sub> (red), SbMP(OMe)<sub>2</sub>.PF<sub>6</sub> (green), SbDMP(OMe)<sub>2</sub>.PF<sub>6</sub> (magenta), and SbTMP(OMe)<sub>2</sub>.PF<sub>6</sub> (violet) in CH<sub>2</sub>Cl<sub>2</sub>.

**Table 1.** Optical and redox data of investigated compounds in CH<sub>2</sub>Cl<sub>2</sub>.

Porphyrin	Absorption λ in nm (log ε in M <sup>-1</sup> cm <sup>-1</sup> )	FWHM of B- band (nm)
ZnTPP	585 (3.32), 547 (4.08), 418 (5.54)	10
SbP(OMe) <sub>2</sub> .PF <sub>6</sub>	592 (4.27), 551 (4.55), 513 (3.72), 421 (5.98)	11
SbMP(OMe) <sub>2</sub> .PF <sub>6</sub>	607 (4.84), 560 (4.62), 523 (4.02), 439 (5.86)	25
SbDMP(OMe) <sub>2</sub> .PF <sub>6</sub>	595 (4.39), 555 (5.01), 514 (4.21), 429 (5.77)	49
SbTMP(OMe) <sub>2</sub> .PF <sub>6</sub>	604 (4.65), 559 (4.84), 519 (4.27), 444 (5.57)	78

(Soret) and four Q-bands. The band positions and molar extinction coefficients of the four free-base porphyrins are comparable suggest that the electronic structure of the porphyrin ring is very similar in all four porphyrins. On the other hand, the antimony(V) porphyrins showed D<sub>4h</sub> symmetry type spectra with one B-band (Soret) and two Q-bands. Unlike the free-base porphyrins, the antimony(V) porphyrins showed significant differences within the series, See Figure 2 and Table 1. The band positions and molar extinction coefficients are considerably different from each other. The SbP(OMe)<sub>2</sub>.PF<sub>6</sub> (red) shows a spectrum with a sharp B-band at 421 nm and two Q-bands at 551 and 592 nm. The full-width half-maxima (FWHM) for B-band was found to be 11 nm. On contrary, the SbMP(OMe)<sub>2</sub>.PF<sub>6</sub> (green) revealed a broad and red-shifted (by 9–18 nm) absorption spectrum with the B- and Q-bands at 439, 560, and 607 nm, respectively. The FWHM for B-band was estimated to be 25 nm, which is double than that of SbP(OMe)<sub>2</sub>.PF<sub>6</sub>. In the case of SbDMP(OMe)<sub>2</sub>.PF<sub>6</sub> (magenta), the characteristic B- and Q-bands appear at 429, 555, and 595 nm. Interestingly, the observed spectrum is redshifted compared to the SbP(OMe)<sub>2</sub>.PF<sub>6</sub>, but blue-shifted relative to the SbMP(OMe)<sub>2</sub>.PF<sub>6</sub>. The FWHM further increased to 49 nm compared to the former two compounds, SbP(OMe)<sub>2</sub>.PF<sub>6</sub> and

SbMP(OMe)<sub>2</sub>.PF<sub>6</sub>. Lastly, the SbTMP(OMe)<sub>2</sub>.PF<sub>6</sub> (violet) spectrum displays the highest spectral broadness and redshifts compared to any of the three former compounds. The B-band of this compound is almost ~150 nm wider with FWHM of 78 nm and centered around 444 nm. The two Q-bands appear at 559 and 604 nm. Similar trends were observed in acetonitrile and toluene, see Figure S10 and Table S15.

To verify the origin of the spectral broadness the UV-visible absorbance was measured as a function of concentration in CH<sub>3</sub>CN and toluene. As shown in Figure S11, the absorbance of SbP(OMe)<sub>2</sub>.PF<sub>6</sub> and SbTMP(OMe)<sub>2</sub>.PF<sub>6</sub> are linearly dependent on the concentration and obey the Beer-Lambert equation. Therefore, the obtained linear curve rules out broadening as a result of aggregation. Hence, the observed spectral broadness is a purely intrinsic property of the studied Sb(V) porphyrins.

To unravel the spectra trends, resonance structures are constructed for Sb(V) porphyrin bearing *meso*-phenyls with *p*- and *m*-methoxy substitutions, see Figure 3. As shown, the *p*-methoxy substitution induces a better effect (push-pull) than the *m*-methoxy group. This is because the *p*-methoxy resonance process builds up negative charge on the *meso*-carbon which ultimately pushed on to the porphyrin central ring. However, it is important to note that this push-pull nature is only feasible in presence of highly oxidized Sb(V) ion. Therefore, it is expected that the electronic structure in SbMP(OMe)<sub>2</sub>.PF<sub>6</sub> and SbTMP(OMe)<sub>2</sub>.PF<sub>6</sub> should be more perturbed than that of SbP(OMe)<sub>2</sub>.PF<sub>6</sub> and SbDMP(OMe)<sub>2</sub>.PF<sub>6</sub>. As predicted, the absorption spectra of the SbMP(OMe)<sub>2</sub>.PF<sub>6</sub> and SbTMP(OMe)<sub>2</sub>.PF<sub>6</sub> were significantly redshifted, whereas no redshift was noticed in SbDMP(OMe)<sub>2</sub>.PF<sub>6</sub> compared to the non-methoxy phenyl substituted SbP(OMe)<sub>2</sub>.PF<sub>6</sub>.

### Computational studies

The electronic structures of the antimony(V) porphyrins were predicted by performing DFT calculations. Figures 4 top row shows optimized structures. The structures were completely optimized to a stationary point on the Born-Oppenheimer potential energy surface using the

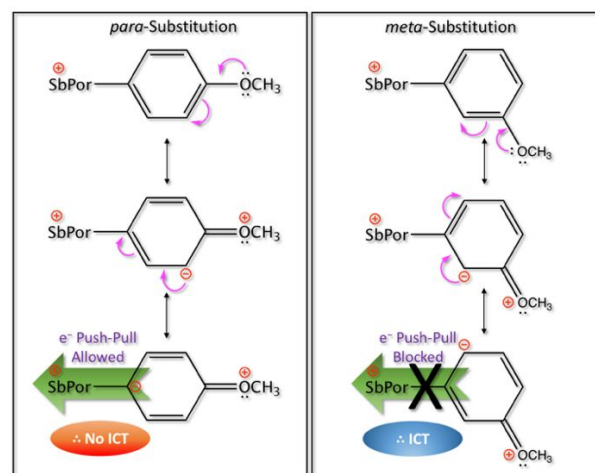


**Figure 3.** Antimony(+5) induced resonance structures of the *para*- and *meta*-methoxy phenyl substituted antimony(V) porphyrins.

B3LYP/GenECP model chemistry, 6-311G(d,p) for H, C, N, and O and def2TZVPP for Sb, as parameterized in the *Gaussian 16* software suite. All the optimized geometries reveal planar porphyrin ring, which is coherent with X-ray structures. The meso-phenyl derivatives form an average dihedral angle of 77°, 70°, 80°, and 80° in  $\text{SbP}(\text{OMe})_2^+$ ,  $\text{SbMP}(\text{OMe})_2^+$ ,  $\text{SbDMP}(\text{OMe})_2^+$ , and  $\text{SbTMP}(\text{OMe})_2^+$ , respectively. On the other note, the axial methoxy units are perfectly perpendicular to the porphyrin plane, however, they are aligned in a way that they break the symmetry of the porphyrin.

Figure 5 illustrates the frontier orbitals of antimony(V) porphyrin. The LUMO and LUMO+1 are localized primarily on the porphyrin ring and no major differences were observed as changing the meso substitutions. However, the HOMO and HOMO-1 showed a very different behaviour than the LUMOs. The HOMO of  $\text{SbP}(\text{OMe})_2^+$  is largely localized on the porphyrin ring and a minor component of HOMO is delocalized over to the meso-phenyl ring. The delocalization gradually increases with increasing the number of methoxy substitutions on the phenyl

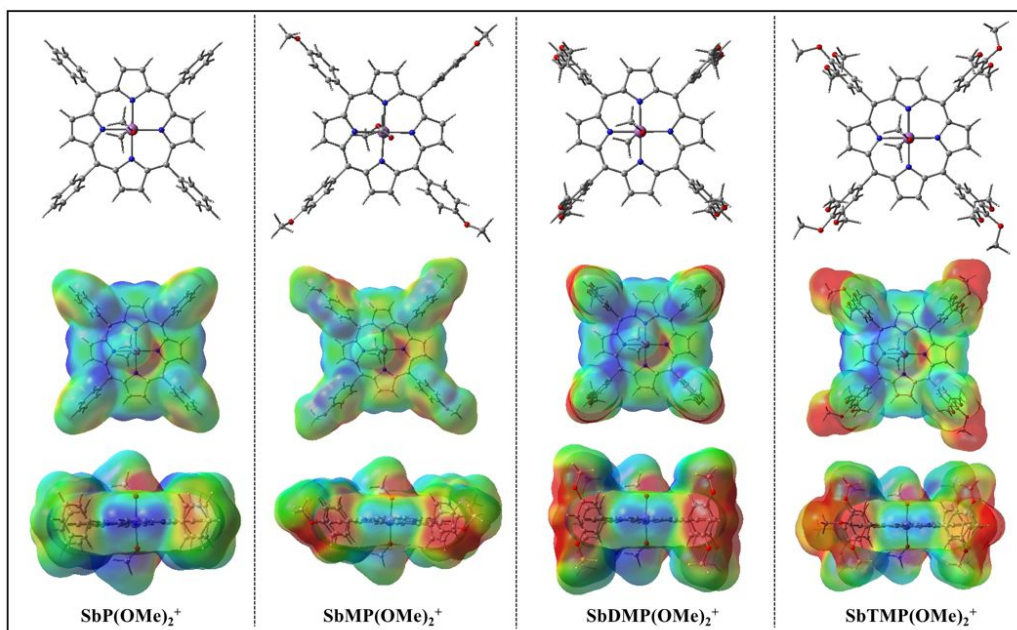


**Figure 4.** Top row: Optimized structures, and Bottom rows: Electrostatic maps of the antimony(V) porphyrin derivatives. Blue = electron acceptor region. Red = electron donor region

	HOMO-1	HOMO	LUMO	LUMO+1
$\text{SbP}(\text{OMe})_2^+$	-8.69 eV	-8.45 eV	-5.69 eV	-5.69 eV
$\text{SbMP}(\text{OMe})_2^+$	-8.24 eV	-7.89 eV	-5.43 eV	-5.43 eV
$\text{SbDMP}(\text{OMe})_2^+$	-8.19 eV	-8.10 eV	-5.60 eV	-5.60 eV
$\text{SbTMP}(\text{OMe})_2^+$	-7.94 eV	-7.87 eV	-5.52 eV	-5.52 eV

**Figure 5.** Calculated frontier molecular orbitals and their energies of the investigated antimony(V) porphyrin derivatives.

## ARTICLE

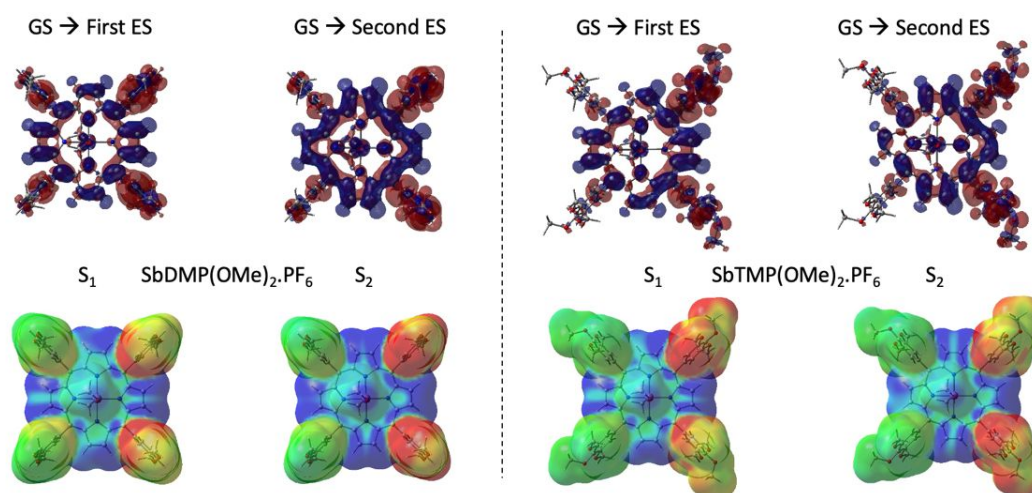


**Figure 6.** Top row: Charge transfer state density difference between ground and first and second excited states. Cyan, ground-state density; purple, excited-state density. Bottom row: Electrostatic potential surface. Red, charge donor region; blue, charge acceptor region; GS, ground state; ES, excited state.

ring, and it becomes maximum in  $\text{SbTMP(OMe)}_2^+$ . The HOMO and HOMO-1 delocalization follows:  $\text{SbTMP(OMe)}_2^+ > \text{SbDMP(OMe)}_2^+ > \text{SbMP(OMe)}_2^+ > \text{SbP(OMe)}_2^+$ . The localized LUMO on the porphyrin ring and delocalized HOMO on the phenyl ring create conditions for push-pull type ICT in the molecule. Based on the frontier orbitals it is expected that the ICT could follow:  $\text{SbTMP(OMe)}_2^+ > \text{SbDMP(OMe)}_2^+ > \text{SbMP(OMe)}_2^+ \approx \text{SbP(OMe)}_2^+$ . From the energies of these frontier molecular orbitals, the HOMO and LUMO gaps were estimated to be 2.74, 2.44, 2.50 and 2.35 eV for  $\text{SbP(OMe)}_2^+$ ,  $\text{SbMP(OMe)}_2^+$ ,  $\text{SbDMP(OMe)}_2^+$ , and  $\text{SbTMP(OMe)}_2^+$ , respectively. The electrostatic potential maps (Figure 4 bottom rows) further support possible ICT process. The blue regions indicate the electron acceptor part while the red regions indicate electron donor part in the molecule. As shown the red colour increases on the phenyl rings with methoxy groups and reached maximum in  $\text{SbTMP(OMe)}_2^+$ . The electron density difference (between ground and excited states) and electrostatic potential maps of the investigated conjugates are calculated by time dependent DFT and are shown in Figure 6, top row. The ground-state charge density of meso-aryl is being transferred to the excited states (S<sub>1</sub> and S<sub>2</sub>) of central antimony(V) porphyrin upon excitation of the porphyrins in  $\text{SbDMP(OMe)}_2^+$  and  $\text{SbTMP(OMe)}_2^+$ . The electrostatic potential maps (Figure 6, bottom row) further compliment this ICT process. The red regions localized on the meso-aryl indicate the loss of electron density, while the blue regions localized on the porphyrin ring are an increase in electron density. In the case of  $\text{SbP(OMe)}_2^+$  and  $\text{SbMP(OMe)}_2^+$  such ICT is not witnessed, this is

exemplified in Figure S12, as the electrostatic potential maps remain green.

### Electrochemistry

Cyclic and differential voltammograms of investigated antimony(V) porphyrins and their corresponding free-base porphyrins were measured in  $\text{CH}_3\text{CN}$  with 0.1 M  $\text{TBA.PF}_6$  and in  $\text{CH}_2\text{Cl}_2$  with 0.1 M  $\text{TBA.ClO}_4$ , respectively. Representative voltammograms are shown in Figures 7 and S13, and the data are summarized in Table 2. The nature of the redox processes is established based on the peak-to-peak separation values, and the cathodic-to-anodic peak current ratio. The voltammogram of free-base porphyrins revealed two reduction and two oxidation processes under our experimental conditions. All of these four processes are found to be reversible and one-electron processes. All the four free-base porphyrins possess very similar reduction potentials. On contrary, the oxidation potentials reveal variations, especially, between *p*-methoxy and *m*-methoxy/*no*-methoxy substituted porphyrins. The  $\text{H}_2\text{MP}$  and  $\text{H}_2\text{TMP}$  are oxidizing by  $\sim 10$ - $100$  mV lower potentials than the  $\text{H}_2\text{P}$  and  $\text{H}_2\text{DMP}$  compounds, which suggest that the HOMO of the  $\text{H}_2\text{MP}$  and  $\text{H}_2\text{TMP}$  have higher electron densities due to *p*-methoxy substitutions. Interestingly, within these two porphyrins the oxidation potentials of  $\text{H}_2\text{MP}$  are  $\sim 100$  mV less positive than  $\text{H}_2\text{TMP}$ . These results are clearly complimenting the DFT and inductive effect from the resonance structures. Figure S14 shows the redox voltammograms of methoxybenzenes in  $\text{CH}_3\text{CN}$  with 0.1 M  $\text{TBA.ClO}_4$  and data are

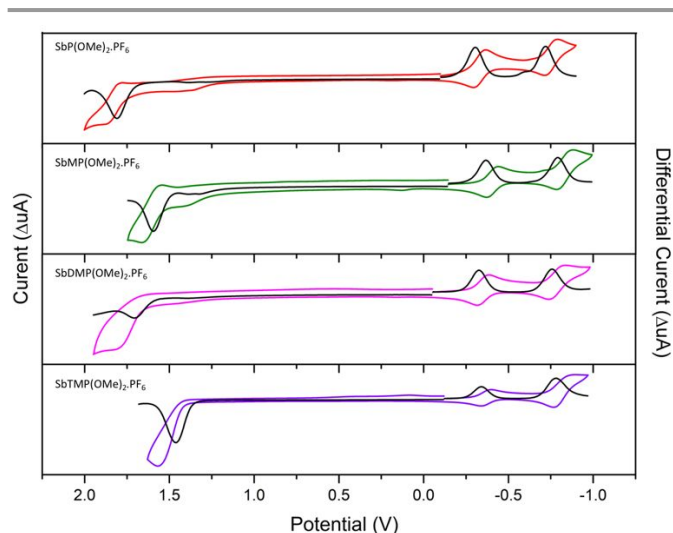


**Figure 7.** Cyclic and differential voltammograms of antimony(V) porphyrins in  $\text{CH}_3\text{CN}$  with 0.1 M TBA.PF<sub>6</sub>. Scan rate 100 mV/s. Pulse period 200 ms. Pulse amplitude 50 mV, Pulse width 50 ms.

**Table 2.** Redox data of the investigated compounds.

Sample	Potentials (V vs SCE)	
	Reduction	Oxidation
H <sub>2</sub> P <sup>a</sup>	-1.17, -1.49	1.01, 1.26
H <sub>2</sub> MP <sup>a</sup>	-1.23, -1.54	0.89, 1.06
H <sub>2</sub> DMP <sup>a</sup>	-1.22, -1.54	1.02, 1.26
H <sub>2</sub> TMP <sup>a</sup>	-1.26, -1.59	1.00, 1.15
SbP(OMe) <sub>2</sub> .PF <sub>6</sub> <sup>b</sup>	-0.33, -0.75	1.78
SbMP(OMe) <sub>2</sub> .PF <sub>6</sub> <sup>b</sup>	-0.34, -0.79	1.60
SbDMP(OMe) <sub>2</sub> .PF <sub>6</sub> <sup>b</sup>	-0.32, -0.76	1.73
SbTMP(OMe) <sub>2</sub> .PF <sub>6</sub> <sup>b</sup>	-0.34, -0.78	1.46
MP <sup>c</sup>	–	1.76
DMP <sup>c</sup>	–	1.50
TMP <sup>c</sup>	–	1.37

<sup>a</sup>in  $\text{CH}_2\text{Cl}_2$  with 0.1 M TBA.ClO<sub>4</sub>. <sup>b</sup>in  $\text{CH}_3\text{CN}$  with 0.1 M TBA.PF<sub>6</sub>. <sup>c</sup>in  $\text{CH}_3\text{CN}$  with 0.1 M TBA.ClO<sub>4</sub>.

summarized in Table 2. The methoxybenzene, 1,3-dimethoxybenzene, and 1,2,3-trimethoxybenzene revealed a one-oxidation irreversible process at 1.76, 1.50, and 1.37 V, respectively. The observed potentials are consistent with their electron densities.

Insertion of Sb(V) ion in the free-base porphyrins reveals dramatic effects on the redox potentials of the resulting antimony(V) porphyrins as they acquire very positive potential compared to their free-base porphyrin counterparts. This is due to the presence of +5 oxidation state of Sb, which makes the porphyrin highly electron-deficient, under these conditions the porphyrins have high oxidation and lower reduction potentials, see Figure 7 and Table 2. The cathodic scan reveals two reduction processes between -0.32 and -0.79 V corresponding to the successive addition of two electrons to the LUMO which

is localized primarily on the porphyrin ring. The two reduction potentials are very similar in all of the four antimony(V) porphyrins, and they were found to be reversible and one-electron processes. The anodic scan of the antimony(V) porphyrins revealed the oxidation process (from DPV curves) at 1.78, 1.60, 1.73, and 1.46 V for SbP(OMe)<sub>2</sub>.PF<sub>6</sub>, SbMP(OMe)<sub>2</sub>.PF<sub>6</sub>, SbDMP(OMe)<sub>2</sub>.PF<sub>6</sub> and SbTMP(OMe)<sub>2</sub>.PF<sub>6</sub>, respectively, and correspond to the removal of electrons from the HOMO. As predicted from the DFT calculations and resonance structures, the HOMO of SbP(OMe)<sub>2</sub>.PF<sub>6</sub> is mainly localized on the electron deficient central porphyrin ring. Therefore, highly positive potential 1.78 V was observed. However, this deficiency was nullified some extent in SbMP(OMe)<sub>2</sub>.PF<sub>6</sub> due to the inductive effect from the meso *p*-methoxyphenyl group, hence, less positive potential 1.60 V was resulted. In the case of SbDMP(OMe)<sub>2</sub>.PF<sub>6</sub>, no inductive effect is feasible, moreover, the HOMO has a substantial contribution from the meso 3,5-trimethoxyphenyl ring. Hence the process becomes irreversible with potential of 1.73 V. Lastly, the SbTMP(OMe)<sub>2</sub>.PF<sub>6</sub> system showed oxidation potential of 1.46 V, which is lowest in the series. This is a result of both the inductive effect and the presence of HOMO on the meso 3,4,5-trimethoxyphenyl ring. Furthermore, oxidation process becomes irreversible and the corresponding currents are much higher than the reduction processes. These trends support the oxidation process occurring on the meso 3,4,5-trimethoxyphenyl ring. Overall, a rich redox chemistry was noticed from the studied porphyrins. The most prominent feature is the high positive potentials for antimony(V) porphyrins. The potentials shifted positively by ~900 mV compared to their corresponding free-base porphyrins.

### Solvatochromism

To envision the ICT character, emission images of antimony(V) porphyrin solutions were taken under ambient light and under UV irradiation (365 nm), see Figure 8. Solution concentrations were kept  $\sim 1 \times 10^{-4}$  M in  $\text{CH}_3\text{CN}$ ,  $\text{CH}_2\text{Cl}_2$ , and toluene. Due to solubility reasons, lower concentrations,  $\sim 2.5 \times 10^{-5}$  M, were maintained in benzene. As shown in Figure 8 (left column) image, each sample has the same colour in four different solvents but has a different colour within the series. Unlike the antimony(V) porphyrin derivatives, their corresponding free-base porphyrins showed almost identical colours in any given solvent, see Figure S15.

Figure 8 (middle column) shows the fluorescence images of the antimony(V) porphyrins in  $\text{CH}_3\text{CN}$ ,  $\text{CH}_2\text{Cl}_2$ , toluene, and benzene solutions under UV light 365 nm. In polar  $\text{CH}_3\text{CN}$  solutions, compounds SbP(OMe)<sub>2</sub>.PF<sub>6</sub> and SbMP(OMe)<sub>2</sub>.PF<sub>6</sub> exhibited a strong fluorescence, whereas the SbDMP(OMe)<sub>2</sub>.PF<sub>6</sub> and SbTMP(OMe)<sub>2</sub>.PF<sub>6</sub> were found to be non-fluorescent. Interestingly, in a moderate polar solvent such as  $\text{CH}_2\text{Cl}_2$ , the fluorescence from SbDMP(OMe)<sub>2</sub>.PF<sub>6</sub> was recovered. However, the SbTMP(OMe)<sub>2</sub>.PF<sub>6</sub> remains as a non-fluorescent compound. In non-polar toluene solutions, the trends were found to be very similar with  $\text{CH}_2\text{Cl}_2$  solutions, that is SbP(OMe)<sub>2</sub>.PF<sub>6</sub>, SbMP(OMe)<sub>2</sub>.PF<sub>6</sub>, and SbDMP(OMe)<sub>2</sub>.PF<sub>6</sub> are

## ARTICLE

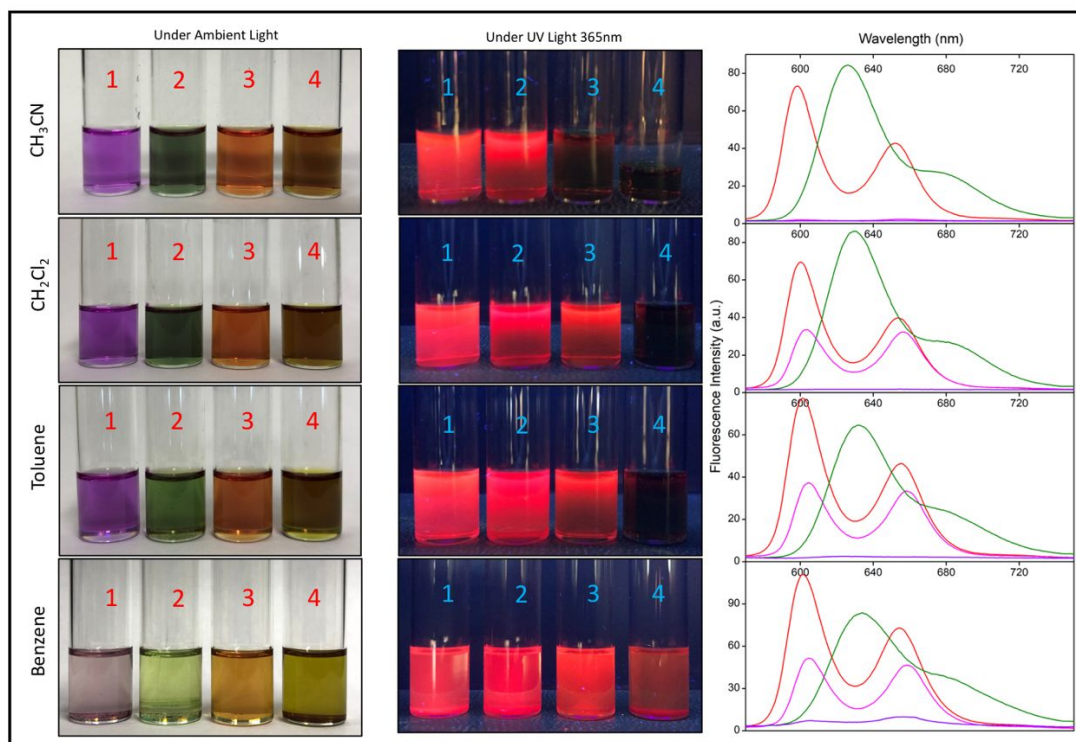


**Figure 8.** Solvatochromism of (1) SbP(OMe)<sub>2</sub>.PF<sub>6</sub>, (2) SbMP(OMe)<sub>2</sub>.PF<sub>6</sub>, (3) SbDMP(OMe)<sub>2</sub>.PF<sub>6</sub> and (4) SbTMP(OMe)<sub>2</sub>.PF<sub>6</sub> in four different solvents under an ambient light (top panel) and 365 nm UV light (middle panel). Far right panel: Steady-state fluorescence spectra of SbP(OMe)<sub>2</sub>.PF<sub>6</sub> (red), SbMP(OMe)<sub>2</sub>.PF<sub>6</sub> (green), SbDMP(OMe)<sub>2</sub>.PF<sub>6</sub> (magenta), and SbTMP(OMe)<sub>2</sub>.PF<sub>6</sub> (violet) in CH<sub>3</sub>CN, CH<sub>2</sub>Cl<sub>2</sub>, Toluene, and Benzene. Excitation wavelength = 550 nm.

fluorescent, and SbTMP(OMe)<sub>2</sub>.PF<sub>6</sub> is non-fluorescent. Remarkably, a slight lowering the polarity, i.e. from toluene to benzene, the SbTMP(OMe)<sub>2</sub>.PF<sub>6</sub> becomes fluorescent, which means all four compounds fluoresce in benzene solutions. The solvent-dependent fluorescence property hints at the presence of the charge transfer character in the molecule.

#### Emission studies

Steady-state fluorescence measurements were carried out in CH<sub>3</sub>CN, CH<sub>2</sub>Cl<sub>2</sub>, toluene, and benzene solvents with excitation wavelengths of 550 nm for free-base and antimony(V) porphyrins. The corresponding data are summarized in Tables S16 and 3. Figure S16 shows the fluorescence spectra of free-base porphyrins, and they all exhibit a very similar spectra and quantum yields ( $\Phi_{\text{flu}}$ ) with two intense emission bands between 630 and 750 nm in all the investigated solvents. However, the most interesting results come from their corresponding Sb(V) porphyrins. As shown in Figure 8 (right column), the fluorescence intensities depend on meso substitution as well as the solvent polarity. In polar CH<sub>3</sub>CN, the SbP(OMe)<sub>2</sub>.PF<sub>6</sub>

compound exhibited an intense spectrum with band positions at 598 and 652 nm. The estimated  $\Phi_{\text{flu}}$  was found to be 0.040 and is comparable to the tetraphenylporphyrinatozinc(II) (ZnP), see Table 3. In the case of SbMP(OMe)<sub>2</sub>.PF<sub>6</sub> the fluorescence spectrum is redshifted by ~30 nm, moreover, the  $\Phi_{\text{flu}}$  is higher than the SbP(OMe)<sub>2</sub>.PF<sub>6</sub>. In contrast, compounds SbDMP(OMe)<sub>2</sub>.PF<sub>6</sub> and SbTMP(OMe)<sub>2</sub>.PF<sub>6</sub> are found to be non-fluorescent. In CH<sub>2</sub>Cl<sub>2</sub> solutions, a similar trend observed for SbP(OMe)<sub>2</sub>.PF<sub>6</sub> and SbMP(OMe)<sub>2</sub>.PF<sub>6</sub>. Interestingly, fluorescence from the SbDMP(OMe)<sub>2</sub>.PF<sub>6</sub> is recovered and the  $\Phi_{\text{flu}}$  found to be 0.024. However, the SbTMP(OMe)<sub>2</sub>.PF<sub>6</sub> compound remains non-fluorescent. In nonpolar toluene solvent, the SbP(OMe)<sub>2</sub>.PF<sub>6</sub> and SbMP(OMe)<sub>2</sub>.PF<sub>6</sub>, and SbDMP(OMe)<sub>2</sub>.PF<sub>6</sub> are found to be fluorescent with high  $\Phi_{\text{flu}}$  values. In contrary, the SbTMP(OMe)<sub>2</sub>.PF<sub>6</sub> is still non-fluorescent. In attempt to recover the fluorescence from the SbTMP(OMe)<sub>2</sub>.PF<sub>6</sub> the spectrum was collected in nonpolar benzene solutions, which is slightly more nonpolar than toluene. The fluorescence was recovered, but the  $\Phi_{\text{flu}}$  calculated to be 0.007. Overall, the results conclude the

## ARTICLE

**Table 3.** Fluorescence quantum yields ( $\Phi_{\text{flu}}$ ), lifetimes ( $\tau_{\text{flu}}$ ), phosphorescence data, first excited singlet state energy ( $E_{0-0}$ ) and triplet state energy (ET) of the antimony(V) porphyrins.

Porphyrin	Fluorescence ( $\lambda$ , nm) <sup>a</sup> ( $\Phi_{\text{flu}}$ ) Average Lifetime ( $\tau$ , ns) (ChiSQ)				Phosphorescence <sup>b</sup> (nm)	$E_{0-0}$ (eV)	$E_{\text{T}}$ <sup>b</sup> (eV)
	CH <sub>3</sub> CN	CH <sub>2</sub> Cl <sub>2</sub>	Toluene	Benzene			
SbP(OMe) <sub>2</sub> .PF <sub>6</sub>	598, 652 (0.040) 1.36 (1.03)	600, 654 (0.038) 1.24 (1.02)	601, 655 (0.045) 1.04 (0.99)	601, 654 (0.043) -	765, 862	2.09 <sup>c</sup>	1.62
SbMP(OMe) <sub>2</sub> .PF <sub>6</sub>	626, 676 (0.057) 1.05 (1.03)	630, 679 (0.058) 0.97 (1.08)	632, 678 (0.048) 0.57 (1.04) <sup>e</sup>	634, 680 (0.044) -	761, 793	2.01 <sup>c</sup>	1.59
SbDMP(OMe) <sub>2</sub> .PF <sub>6</sub>	600, 658 (0.003) -	603, 656 (0.024) 1.02 (1.02)	605, 658 (0.026) 0.91 (1.07)	605, 658 (0.023) -	753, 837	2.10 <sup>c</sup>	1.65
SbTMP(OMe) <sub>2</sub> .PF <sub>6</sub>	NF -	NF -	NF 0.27 (1.12) <sup>e</sup>	614, 659 (0.007)	768, 850	1.99 <sup>d</sup>	1.61
ZnTPP	603, 657 (0.044)	596, 645 (0.036)	597, 648 (0.047)	597, 647 (0.045)	789, 880	2.14 <sup>c</sup>	1.57

<sup>a</sup>Fluorescence quantum yields ( $\Phi_{\text{flu}}$ ) were calculated by the steady-state comparative method using tetraphenylporphyrinatozinc(II) (ZnTPP,  $\Phi_{\text{flu}} = 0.036$  in CH<sub>2</sub>Cl<sub>2</sub>)<sup>38</sup> as reference sample. <sup>b</sup>THF:CH<sub>2</sub>Cl<sub>2</sub>:1,2-dibromoethane = 65%:22%:13% at 77K. <sup>c</sup>in CH<sub>2</sub>Cl<sub>2</sub>. <sup>d</sup>in Benzene. NF: Negligible Fluorescence. <sup>e</sup>Biexponential fit.

following: (i) the solvent dependent fluorescence studies are very much consistent with the trends that were noticed in solvatochromism studies, and (ii) solvent dependency indicates the presence of the ICT character in the studied systems, particularly, in SbDMP(OMe)<sub>2</sub>.PF<sub>6</sub>, and SbTMP(OMe)<sub>2</sub>.PF<sub>6</sub>. Figure S17 displays the phosphorescence spectra of investigated compounds at 77 K. The observed band positions are summarized in Table S15 and Table 3. The free-base porphyrin phosphorescence bands have a low signal-to-noise ratio, but the antimony(V) porphyrin derivatives showed intense spectra and have distinctive features between 725 to 900 nm.

Time-resolved fluorescence studies of antimony(V) porphyrin were measured in CH<sub>3</sub>CN, CH<sub>2</sub>Cl<sub>2</sub>, and toluene. The samples were excited at 561 nm and the emission was collected at the high-energy fluorescence band. The representative fluorescence decay profiles are illustrated in Figure S18 and the lifetime data were summarized in Table 3. The decay profiles of antimony(V) porphyrin in toluene and were able to fit the mono-exponential expression except for the SbMP(OMe)<sub>2</sub>.PF<sub>6</sub> and SbTMP(OMe)<sub>2</sub>.PF<sub>6</sub>, which decays bi-exponentially with a minor component of a very long-lived lifetime. The average value was considered for discussion purposes. The lifetimes of antimony(V) porphyrin were found to be in the following order: SbP(OMe)<sub>2</sub>.PF<sub>6</sub> > SbDMP(OMe)<sub>2</sub>.PF<sub>6</sub> > SbMP(OMe)<sub>2</sub>.PF<sub>6</sub> > SbTMP(OMe)<sub>2</sub>.PF<sub>6</sub>.

### Energetics

The redox potentials can be used in combination with optical data to construct the energy level diagram of the states involved in possible charge-transfer processes. Figure 9 summarizes the

energy levels of the investigated compounds. The energies of the lowest excited singlet states ( $E_{0-0}$ ) of antimony(V) porphyrin were calculated from the overlap of the absorption and fluorescence data, see Figure S19. For SbP(OMe)<sub>2</sub>.PF<sub>6</sub>, SbMP(OMe)<sub>2</sub>.PF<sub>6</sub> and SbDMP(OMe)<sub>2</sub>.PF<sub>6</sub> solvent CH<sub>2</sub>Cl<sub>2</sub>, whereas for SbTMP(OMe)<sub>2</sub>.PF<sub>6</sub> solvent benzene was used. The triplet state energies were obtained from the positions of the phosphorescence bands. The energy of the CT state above the ground state can be roughly estimated as the difference between the oxidation of free methoxyphenyl derivative and first reduction potentials of antimony(V) porphyrin. From the electrostatic potential maps, it was found out the electron-rich and electron-poor regions are mainly centered on the meso aryl rings and central porphyrin ring, respectively, in the case of SbMP(OMe)<sub>2</sub>.PF<sub>6</sub>, SbDMP(OMe)<sub>2</sub>.PF<sub>6</sub> and SbTMP(OMe)<sub>2</sub>.PF<sub>6</sub>. Therefore, it is reasonable to calculate the charge-transfer state energies from the redox potentials.

### Femtosecond transient absorption studies

The energy level diagram shown in Figure 9 revealed the possibility of intramolecular charge transfer (ICT) in SbDMP(OMe)<sub>2</sub>.PF<sub>6</sub> and SbTMP(OMe)<sub>2</sub>.PF<sub>6</sub> having meso methoxyphenyl substituents. Steady-state fluorescence quenching and diminished lifetimes as a function of number of methoxy groups on the phenyl ring and of solvent polarity support such a claim. The data and pictures shown in Figure 8 clearly demonstrate the occurrence of ICT in nonpolar toluene for SbTMP(OMe)<sub>2</sub>.PF<sub>6</sub>, and for SbDMP(OMe)<sub>2</sub>.PF<sub>6</sub> and SbTMP(OMe)<sub>2</sub>.PF<sub>6</sub> in polar CH<sub>3</sub>CN. To seek evidence for such a process, femtosecond transient absorption (fs-TA) spectral studies were performed both in toluene and CH<sub>3</sub>CN, as shown in Figures 10 and 11. First, in SbMP(OMe)<sub>2</sub>.PF<sub>6</sub>,

## ARTICLE

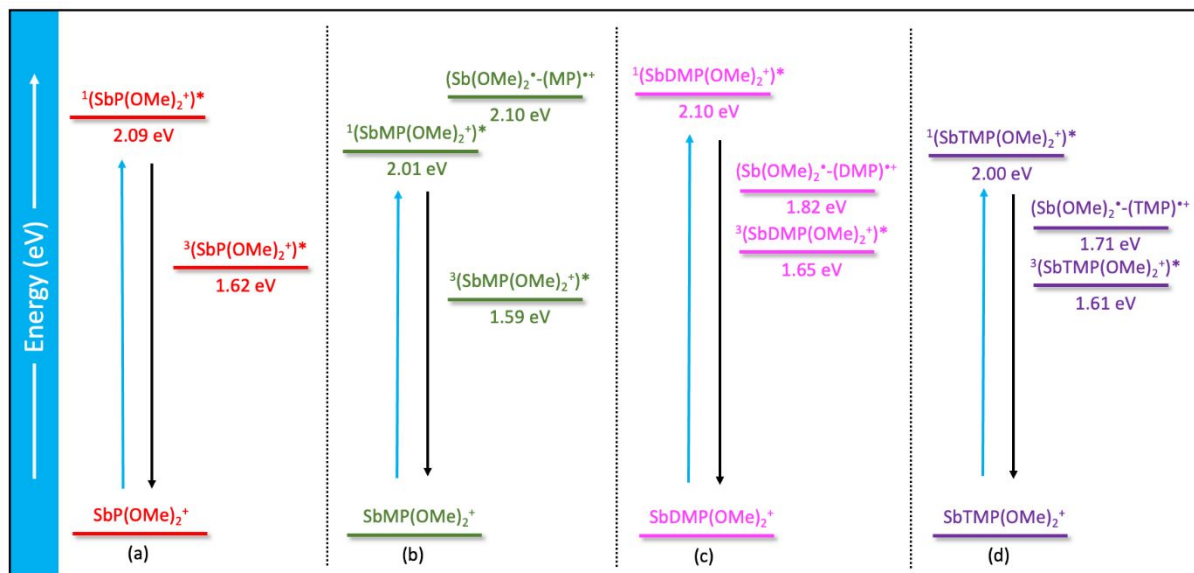


Figure 9. Calculated energy level diagram of (a)  $\text{SbP}(\text{OMe})_2\cdot\text{PF}_6$ , (b)  $\text{SbMP}(\text{OMe})_2\cdot\text{PF}_6$ , (c)  $\text{SbDMP}(\text{OMe})_2\cdot\text{PF}_6$ , and (d)  $\text{SbTMP}(\text{OMe})_2\cdot\text{PF}_6$  in  $\text{CH}_3\text{CN}$ .

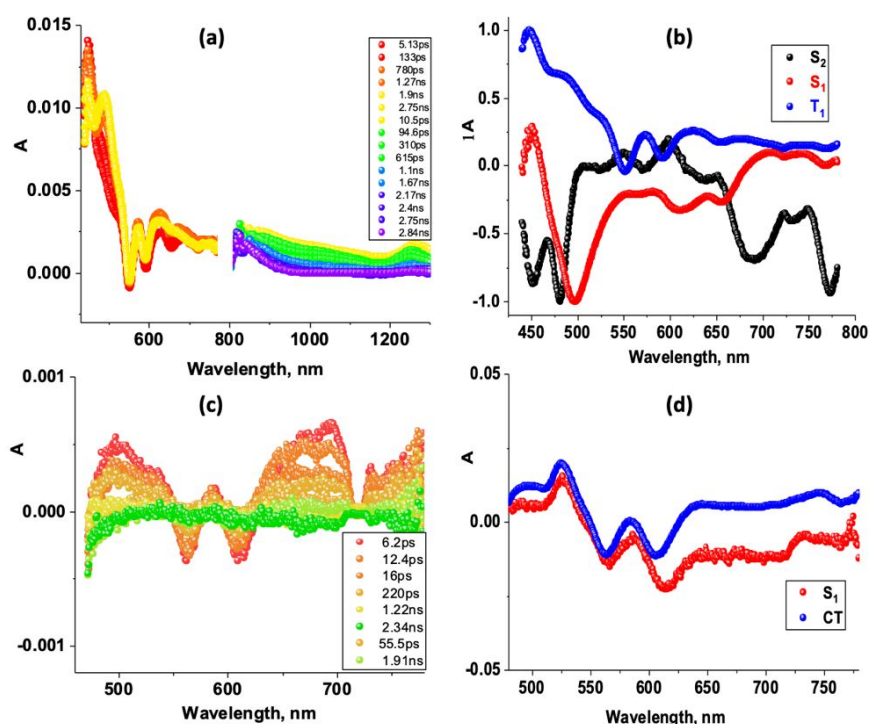


Figure 10. *fs*-TA absorption spectra at the indicated delay times of (a)  $\text{SbP}(\text{OMe})_2\cdot\text{PF}_6$  and (c)  $\text{SbTMP}(\text{OMe})_2\cdot\text{PF}_6$  in oxygen-free toluene at the Soret band excitation. (b) and (d) show the corresponding decay associated spectra generated from global analysis

$\text{SbDMP}(\text{OMe})_2\cdot\text{PF}_6$  and  $\text{SbTMP}(\text{OMe})_2\cdot\text{PF}_6$  were chemically reduced using cobaltocene in  $\text{CH}_3\text{CN}$  to spectrally characterize

the reduced antimony porphyrins. Figure S20 shows such spectral data. In all cases, the addition of cobaltocene resulted

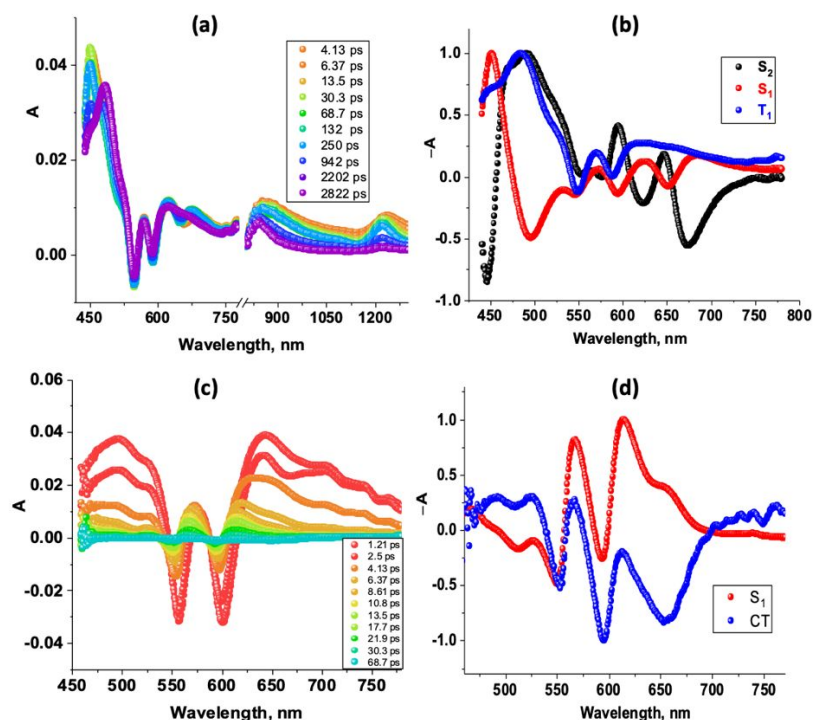
in new peaks, the first one is a broad peak centered around 500 nm, and an additional two peaks at 698 and 768 nm. The appearance of new peaks in this spectral range during transient spectral measurements would support the ICT process in these push-pull antimony porphyrins.

Figure 10a shows the *fs*-TA spectra of SbP(OMe)<sub>2</sub>.PF<sub>6</sub> at the indicated delay times in toluene at Soret band (S<sub>2</sub>) excitation. The S<sub>2</sub> → S<sub>1</sub> internal conversion followed by solvent relaxation of the S<sub>1</sub> state occurred within the first few ps. The S<sub>1</sub> state was characterized by excited-state absorption (ESA) peaks at 450, 572, and 624 nm. In addition, a near-IR peak at 1260 nm was observed, and based on its similarity to other tetraarylporphyrins,<sup>39,40</sup> this has been attributed to the S<sub>1</sub> → S<sub>2</sub> transition. In addition to this, negative signals at 550, 592, and 654 nm were also observed. By comparison with the earlier discussed absorption and fluorescence spectra, the 550 nm peak to the ground state bleaching (GSB), 592 nm peak to both GSB and stimulated emission (SE), and the 654 nm peak to SE was assigned. The decay and recovery of the positive and negative peaks were accompanied by new peaks at 492, 652 (broad peak covering 560–710 nm range), and 848 nm. As no ICT was expected for this compound, the new spectrum was attributed to the T<sub>1</sub> state formed via the process of intersystem crossing (ISC). To analyse the *fs*-TA spectral data, decay-associated spectra (DAS) were generated from global target analysis. A sequential three-component model representing S<sub>2</sub> → S<sub>1</sub> → T<sub>1</sub> states was utilized, as shown in Figure 10b. S<sub>2</sub> with a lifetime of 0.9 ps, S<sub>1</sub> state with a lifetime of 1.0 ns and T<sub>1</sub> state with a lifetime of > 3 ns was obtained. To confirm S<sub>1</sub> → T<sub>1</sub> conversion, the nanosecond transient absorption (*ns*-TA) spectrum of SbP(OMe)<sub>2</sub>.PF<sub>6</sub> was also recorded, as shown in Figure S21a that revealed broad spectral features

corresponding to T<sub>1</sub> → T<sub>n</sub> transition in the 560–720 nm range. From decay analysis, the lifetime of the T<sub>1</sub> state was found to be 9.6 μs.

The *fs*-TA spectra of SbTMP(OMe)<sub>2</sub>.PF<sub>6</sub>, expected to show ICT based on previous discussions, is shown in Figure 10c. The spectral features were drastically different from what was observed in the case of SbP(OMe)<sub>2</sub>.PF<sub>6</sub>. Rapid decay/recovery of the peaks corresponding to the S<sub>1</sub> state revealed spectral features expected for the ICT state. These ESA peaks corresponding to the ICT state were located at 500, 695, and 770 nm (see spectrum at 6.2 ps delay time). Although energetically feasible, further relaxation of the ICT state peaks did not populate the T<sub>1</sub> state, likely due to the large energy gap as predicted by the energy gap law.<sup>41</sup> Further, DAS were generated for data analysis yielded a S<sub>1</sub> lifetime of 2.9 ps and ICT lifetime of 0.25 ns (see Figure 10d). As expected, *ns*-TA spectra were very poorly resolved and hence such data is not shown. The *fs*-TA spectra of SbMP(OMe)<sub>2</sub>.PF<sub>6</sub> and SbDMP(OMe)<sub>2</sub>.PF<sub>6</sub> is shown in Figure S22 along with their corresponding DAS. Spectral features were close to that of SbP(OMe)<sub>2</sub>.PF<sub>6</sub>, that is sequential formation of S<sub>2</sub> → S<sub>1</sub> → T<sub>1</sub> states without much evidence of ICT. Lifetimes of the S<sub>1</sub> states agreed well with the fluorescence lifetime data. The T<sub>1</sub> state of SbDMP(OMe)<sub>2</sub>.PF<sub>6</sub> was also characterized by *ns*-TA in toluene (Figure S21c) which revealed a lifetime of 11.8 μs (see Figure S21d for the decay curve).

Next, ICT features were probed in polar CH<sub>3</sub>CN. Both SbDMP(OMe)<sub>2</sub>.PF<sub>6</sub> and SbTMP(OMe)<sub>2</sub>.PF<sub>6</sub> is expected to show ICT while SbP(OMe)<sub>2</sub>.PF<sub>6</sub> and SbMP(OMe)<sub>2</sub>.PF<sub>6</sub> are expected to behave like simple Sb(V) porphyrins. Figure 11a shows the *fs*-TA



**Figure 11.** *fs*-TA absorption spectra at the indicated delay times of (a) SbP(OMe)<sub>2</sub>.PF<sub>6</sub> and (c) SbTMP(OMe)<sub>2</sub>.PF<sub>6</sub> in oxygen-free CH<sub>3</sub>CN at the Soret band excitation. (b) and (d) show the corresponding decay associated generated from global analysis.

## ARTICLE

at the indicated delay time of  $\text{SbP}(\text{OMe})_2\text{PF}_6$  in  $\text{CH}_3\text{CN}$  at the Soret band excitation. The spectral features were like those observed in toluene. That is, ESA peaks at 450, 622, 676, and 1234 nm were observed. In addition, negative peaks at 548, 590, and 650 nm related to GSB and SE were observed. Decay/recovery of the positive and negative peaks was associated with new peaks with maxima at 486, 663, and 840 nm attributable to the  $T_1$  state. DAS generated based on  $S_2 \rightarrow S_1 \rightarrow T_1$  model (see Figure 11b) revealed a lifetime of 2.5 ps for  $S_2$  state, 0.99 ns for  $S_1$  state, and > 3 ns for  $T_1$  state. The lifetime of the  $S_1$  state agreed well with the fluorescence lifetime. *ns*-TA characterization of the triplet state (see Figure S23a) was also performed. In the visible region, the spectra revealed two main peaks at 598 and 654 nm due to  $T_1 \rightarrow T_n$  transitions. The lifetime of the  $T_1$  state was found to be 3.42  $\mu\text{s}$  relatively shorter than that observed in toluene (see Figure S23b for decay curve).

In contrast to  $\text{SbP}(\text{OMe})_2\text{PF}_6$ , *fs*-TA spectra of  $\text{SbTMP}(\text{OMe})_2\text{PF}_6$  revealed ICT in  $\text{CH}_3\text{CN}$  as shown in Figure 11c. Clear spectral features of ICT state were evident within a ps, and ICT state relaxation to the ground state (not the  $T_1$  state) was also rapid, as expected in the polar solvent. DAS shown in Figure 11d, yielded a lifetime for  $S_1$  state 2.7 ps and that of the ICT state of 6.2 ps. As shown in Figures S24a and b, *fs*-TA spectral data on  $\text{SbMP}(\text{OMe})_2\text{PF}_6$  revealed no evidence of ICT where the data could be fitted to on  $S_2 \rightarrow S_1 \rightarrow T_1$  model. Interestingly, unlike in toluene, in the case of  $\text{SbDMP}(\text{OMe})_2\text{PF}_6$ , clear evidence of ICT was observed (see Figure S24c). That is, changing the polarity of the solvent promoted ICT in the case of  $\text{SbDMP}(\text{OMe})_2\text{PF}_6$ . A lifetime of 3.3 ps for the  $S_1$  state and 20.8 ps for the ICT state were obtained from DAS analysis (see Figure S24d).

## Experimental section

### Synthesis

The chemicals and solvents utilized in this study were purchased from Alfa-Aesar, Fisher Chemical, Acros Organics, Sigma-Aldrich, Tokyo Chemical Industry (TCI), or Accela and were used as received. Chromatographic materials were purchased from SiliCycle or Sigma-Aldrich. Synthesis of  $\text{H}_2\text{P}$  is reported elsewhere.<sup>36</sup> The other compounds used in this study were prepared as described in the supporting information or below sections.

#### Synthesis of axial dimethoxyantimony(V) porphyrins.

Dichloroantimony(V) porphyrin (0.113 mmol) was dissolved in a mixture of 2 mL pyridine, 10 mL methanol, and 10 mL chloroform. This solution was flushed with  $\text{N}_2$  for 10 min, then

the solution was heated to 70°C and stirred for 2 – 72 h under a nitrogen atmosphere. The solvent was removed under reduced pressure and the residue was purified by alumina column chromatography. The column was eluted first with  $\text{CH}_2\text{Cl}_2$  to remove the free-base and then with  $\text{CH}_2\text{Cl}_2:\text{CH}_3\text{OH}$  (= 99:1 to 93:7, see below for more details) to elute the product. The solvent was removed *via* evaporation and the product was converted to a  $\text{PF}_6$  salt by dissolving it in 5 mL methanol and adding 200 mg  $\text{NH}_4\text{PF}_6$ . The product was precipitated by the addition of 25 mL water and collected via vacuum filtration and vacuum dried.

***SbP(OMe)<sub>2</sub>PF<sub>6</sub>***: Reaction time 2 h.  $\text{CH}_2\text{Cl}_2:\text{CH}_3\text{OH}$  (= 95:5) eluent was used for column to collect the product. Yield = 92 mg (86%).  $^1\text{H}$  NMR ( $\text{CDCl}_3$ , 400 MHz):  $\delta$ , ppm 9.55 (8H, s), 8.33 (8H, d,  $J$  = 7.08 Hz), 7.96 (12H, m), -2.18 (6H, s).  $^{13}\text{C}$  NMR ( $\text{CDCl}_3$ , 100 MHz):  $\delta$ , ppm 146.2, 138.3, 135.0, 134.0, 130.1, 128.1, 123.2, 45.9.  $^{31}\text{P}$  NMR ( $\text{CDCl}_3$ , 162 MHz):  $\delta$ , ppm -144.65 (1P, sept,  $J$  = 712.69 Hz).  $^{19}\text{F}$  NMR ( $\text{CDCl}_3$ , 377 MHz):  $\delta$ , ppm -74.07 (6F, d,  $J$  = 712.52 Hz). ESI MS:  $m/z$  795.1454 for  $[\text{M} - \text{PF}_6]^+$ , calculated 795.1714 for  $\text{C}_{46}\text{H}_{34}\text{N}_4\text{O}_2\text{Sb}^+$  X-ray quality crystals grown by using vapor diffusion of pentane into sample solutions in chloroform. Formula =  $\text{C}_{46}\text{H}_{34}\text{F}_6\text{N}_4\text{O}_2\text{PSb}\cdot 3(\text{Chloroform})$ ,  $M_r$  = 1299.59, monoclinic,  $P2_1/n$ ,  $a$  = 12.4250(2) Å,  $b$  = 26.1150(5) Å,  $c$  = 17.3913(4) Å,  $\beta$  = 108.590(2)°,  $\alpha$  =  $\gamma$  = 90°,  $V$  = 5348.67(19) Å<sup>3</sup>,  $T$  = 229.99(12) K,  $Z$  = 4, 48200 reflections measured, 11477 unique ( $R_{int}$  = 0.0471) which were used in all calculations. The final  $R_1$  was 0.0746 ( $I > 2(I)$ ) and  $wR_2$  was 0.1890 (all data).

***SbMP(OMe)<sub>2</sub>PF<sub>6</sub>***. Reaction time 48 h.  $\text{CH}_2\text{Cl}_2:\text{CH}_3\text{OH}$  (= 97:3) eluent was used for column to collect the product. Yield: 111 mg (93%).  $^1\text{H}$  NMR ( $\text{CDCl}_3$ , 400 MHz):  $\delta$ , ppm 9.57 (8H, s), 8.25 (8H, d,  $J$  = 8.44 Hz), 7.46 (8H, d,  $J$  = 8.48 Hz), 4.16 (12H, s), -2.17 (6H, s).  $^{13}\text{C}$  NMR ( $\text{CDCl}_3$ , 100 MHz):  $\delta$ , ppm 161.2, 146.5, 136.4, 133.9, 130.7, 123.0, 113.8, 56.0, 45.9.  $^{31}\text{P}$  NMR ( $\text{CDCl}_3$ , 162 MHz):  $\delta$ , ppm -144.55 (1P, sept,  $J$  = 712.29 Hz).  $^{19}\text{F}$  NMR ( $\text{CDCl}_3$ , 377 MHz):  $\delta$ , ppm -73.94 (6F, d,  $J$  = 712.52 Hz). ESI MS:  $m/z$  915.1753 for  $[\text{M} - \text{PF}_6]^+$ , calculated 915.2137 for  $\text{C}_{50}\text{H}_{42}\text{N}_4\text{O}_6\text{Sb}^+$  X-ray quality crystals grown from slow evaporation of acetone from acetone/water solution of the sample. Formula =  $\text{C}_{50}\text{H}_{42}\text{F}_6\text{N}_4\text{O}_6\text{PSb}\cdot 2(\text{Acetone})$ ,  $M_r$  = 1177.75, monoclinic,  $C2/c$ ,  $a$  = 30.6284(7) Å,  $b$  = 10.75280(10) Å,  $c$  = 20.9262(5) Å,  $\beta$  = 132.011(4)°,  $\alpha$  =  $\gamma$  = 90°,  $V$  = 5120.8(3) Å<sup>3</sup>,  $T$  = 219.99(11) K,  $Z$  = 4, 40217 reflections measured, 5552 unique ( $R_{int}$  = 0.0376) which were used in all calculations. The final  $R_1$  was 0.0369 ( $I > 2(I)$ ) and  $wR_2$  was 0.1060 (all data).

***SbDMP(OMe)<sub>2</sub>PF<sub>6</sub>***: Reaction time 21 h.  $\text{CH}_2\text{Cl}_2:\text{CH}_3\text{OH}$  (= 99:1) eluent was used for column to collect the product. Yield: 116 mg (87%).  $^1\text{H}$  NMR ( $\text{CDCl}_3$ , 400 MHz):  $\delta$ , ppm 9.62 (8H, s), 7.50 (8H, d,  $J$  = 2.24 Hz), 7.03 (4H, t,  $J$  = 2.22 Hz), 4.02 (24H, s), -2.13 (6H, s).  $^{13}\text{C}$  NMR ( $\text{CDCl}_3$ , 100 MHz):  $\delta$ , ppm 159.8, 146.1, 140.2,

133.9, 122.7, 114.8, 101.9, 56.1, 46.1.  $^{31}\text{P}$  NMR ( $\text{CDCl}_3$ , 162 MHz):  $\delta$ , ppm -145.06 (sept,  $J = 712.69$  Hz).  $^{19}\text{F}$  NMR ( $\text{CDCl}_3$ , 377 MHz):  $\delta$ , ppm -73.97 (6F, d,  $J = 712.71$  Hz). ESI MS:  $m/z$  1035.2472 for  $[\text{M} - \text{PF}_6]^+$ , calculated 1035.2560 for  $\text{C}_{54}\text{H}_{50}\text{N}_4\text{O}_{10}\text{Sb}^+$ . X-ray quality crystals grown by using vapor diffusion of pentane into sample solutions in ethylacetate:methanol (= 90:10). Formula =  $\text{C}_{54}\text{H}_{50}\text{F}_6\text{N}_4\text{O}_{10}\text{PSb} \cdot 3(\text{pentane})$ ,  $M_r = 1398.13$ , Monoclinic,  $C 1 2/c 1$ ,  $a = 15.21938(12)$  Å,  $b = 25.80070(18)$  Å,  $c = 45.1560(4)$  Å,  $\alpha = 90^\circ$ ,  $\beta = 90.6426(8)^\circ$ ,  $\gamma = 90^\circ$ ,  $V = 17730.3(2)$  Å $^3$ ,  $T = 150.00(10)$  K,  $Z = 12$ , 73318 reflections measured, 18893 unique ( $R_{\text{int}} = 0.0423$ ) which were used in all calculations. The final  $R_1$  was 0.0471 ( $I > 2(I)$ ) and  $wR_2$  was 0.1243 (all data).

**SbTMP(OMe) $_2$ PF $_6$** : Reaction time 72 h.  $\text{CH}_2\text{Cl}_2:\text{CH}_3\text{OH}$  (= 93:7) eluent was used for column to collect the product. Yield: 132 mg (90%).  $^1\text{H}$  NMR ( $\text{CDCl}_3$ , 400 MHz):  $\delta$ , ppm 9.64 (8H, s), 7.61 (8, s), 4.23 (12H, s), 4.03 (24H, s), -2.05 (6H, s).  $^{13}\text{C}$  NMR ( $\text{CDCl}_3$ , 100 MHz):  $\delta$ , ppm 152.4, 146.4, 139.5, 133.9, 133.8, 122.9, 113.8, 61.5, 56.9, 46.4.  $^{31}\text{P}$  NMR ( $\text{CDCl}_3$ , 162 MHz):  $\delta$ , ppm -145.29 (1P, sept,  $J = 713.10$  Hz).  $^{19}\text{F}$  NMR ( $\text{CDCl}_3$ , 377 MHz):  $\delta$ , ppm -73.82 (6F, d,  $J = 712.97$  Hz). ESI MS:  $m/z$  1155.2711 for  $[\text{M} - \text{PF}_6]^+$ , calculated 1155.2982 for  $\text{C}_{58}\text{H}_{58}\text{N}_4\text{O}_{14}\text{Sb}^+$  X-ray quality crystals grown by using vapor diffusion of pentane into sample solutions in chloroform. Formula =  $\text{C}_{58}\text{H}_{58}\text{F}_6\text{N}_4\text{O}_{14}\text{PSb} \cdot 2(\text{Chloroform})$ ,  $M_r = 1540.54$ , triclinic,  $P-1$ ,  $a = 8.52553(12)$  Å,  $b = 14.3097(2)$  Å,  $c = 14.55804(17)$  Å,  $\alpha = 104.0630(11)^\circ$ ,  $\beta = 103.8304(11)^\circ$ ,  $\gamma = 102.0038(12)^\circ$ ,  $V = 1604.74(4)$  Å $^3$ ,  $T = 229.99(11)$  K,  $Z = 1$ , 24477 reflections measured, 6858 unique ( $R_{\text{int}} = 0.0529$ ) which were used in all calculations. The final  $R_1$  was 0.0618 ( $I > 2(I)$ ) and  $wR_2$  was 0.1647 (all data).

## Conclusions

A simple but novel antimony(V) porphyrin series has been designed to investigate the photophysical properties as a function of meso-substitution. The absorption studies indicate that the electronic structure of the molecule strongly depends on the meso-substitution ring. The p-methoxy substituted antimony(V) porphyrin ( $\text{SbMP}(\text{OMe})_2^+$  and  $\text{SbTMP}(\text{OMe})_2^+$ ) showed significant red-shifted absorption spectra than  $\text{SbP}(\text{OMe})_2^+$  and  $\text{SbDMP}(\text{OMe})_2^+$ . The oxidation potentials also reflect this trend in electrochemical studies as the  $\text{SbMP}(\text{OMe})_2^+$  and  $\text{SbTMP}(\text{OMe})_2^+$  undergo oxidation at lower potentials than  $\text{SbP}(\text{OMe})_2^+$  and  $\text{SbDMP}(\text{OMe})_2^+$ . Interestingly, the reduction potentials are almost unaffected by varying the position and number of methoxy groups on the phenyl ring. The most intriguing results were observed from steady-state emission and solvatochromism studies. The fluorescence intensity strongly depends on the meso-substitution and solvent polarity. The  $\text{SbP}(\text{OMe})_2^+$  and  $\text{SbMP}(\text{OMe})_2^+$  were found strongly fluorescent in all the investigated solvents. However, the fluorescence from  $\text{SbDMP}(\text{OMe})_2^+$  and  $\text{SbTMP}(\text{OMe})_2^+$  is strongly solvent dependant, which reveals a charge transfer behaviour. The insertion of Sb(V) ion in free-base porphyrin induces unequal distribution of electron density in the resulting antimony(V) porphyrin. This results in a push-pull style ICT in the

molecule, and it reaches a maximum in the  $\text{SbTMP}(\text{OMe})_2^+$  where the electron density difference between the center and peripheral is at its peak. The ICT is so strong in  $\text{SbTMP}(\text{OMe})_2^+$ , it was even manifested in nonpolar toluene solvent. From the transient studies, it was found that the ICT process in these porphyrins occurs on picoseconds time scale. The studied series also showed that the position of the methoxy group is important to induce the ICT process. The ICT can be turned on and off by choosing the position of methoxy substitutions on the meso-aryl unit. Overall, the investigated series provides an excellent opportunity to understand the photophysical properties of antimony(V) porphyrins as a function of meso-substitutions. Currently, we are further testing the design principle and the induced ICT process in other main-group porphyrin derivatives.

## Conflicts of interest

There are no conflicts to declare.

## Acknowledgements

This work was supported by Grant-in-Aid (GIA No. 380228 to PPK) and SEED Grant (to PPK) from the University of Minnesota Duluth and by the National Science Foundation (2000988 to FD). The authors also acknowledge NSF-MRI Program (CHE-1726652), and the University of North Texas for supporting the acquisition of the Rigaku XtaLAB Synergy-S X-ray diffractometer. The computational work was completed at the Holland Computing Center of the University of Nebraska, which receives support from the Nebraska Research Initiative.

## Notes and references

- 1 M. K. Chahal, A. Liyanage, A. Z. Alsaleh, P. A. Karr, J. P. Hill and F. D'Souza, *Chem. Sci.*, 2021, **12**, 4925–4930.
- 2 B. Sekaran, Y. Jang, R. Misra and F. D'Souza, *Chem. - A Eur. J.*, 2019, **25**, 12991–13001.
- 3 H. Hayashi, A. S. Touchy, Y. Kinjo, K. Kurotobi, Y. Toude, S. Ito, H. Saarenpää, N. V. Tkachenko, H. Lemmetyinen and H. Imahori, *ChemSusChem*, 2013, **6**, 508–517.
- 4 I. Zegkinoglou, M. E. Ragoussi, C. D. Pemmaraju, P. S. Johnson, D. F. Pickup, J. E. Ortega, D. Prendergast, G. De La Torre and F. J. Himpsel, *J. Phys. Chem. C*, 2013, **117**, 13357–13364.
- 5 J. Zhang, J. Z. Zhang, H. Bin Li, Y. Wu, Y. Geng and Z. M. Su, *Phys. Chem. Chem. Phys.*, 2014, **16**, 24994–25003.
- 6 M. J. Lee, K. D. Seo, H. M. Song, M. S. Kang, Y. K. Eom, H. S. Kang and H. K. Kim, *Tetrahedron Lett.*, 2011, **52**, 3879–3882.
- 7 Z. Parsa, S. S. Naghavi and N. Safari, *J. Phys. Chem. A*, 2018, **122**, 5870–5877.
- 8 T. Bessho, S. M. Zakeeruddin, C. Y. Yeh, E. W. G. Diau and M. Grätzel, *Angew. Chemie - Int. Ed.*, 2010, **49**, 6646–6649.
- 9 A. Yella, C. L. Mai, S. M. Zakeeruddin, S. N. Chang, C. H. Hsieh, C. Y. Yeh and M. Grätzel, *Angew. Chemie - Int. Ed.*,

## Article

- 2014, **53**, 2973–2977.
- 10 S. Mathew, A. Yella, P. Gao, R. Humphry-Baker, B. F. E. Curchod, N. Ashari-Astani, I. Tavernelli, U. Rothlisberger, M. K. Nazeeruddin and M. Grätzel, *Nat. Chem.*, 2014, **6**, 242–247.
- 11 T. Kim, J. Kim, H. Mori, S. Park, M. Lim, A. Osuka and D. Kim, *Phys. Chem. Chem. Phys.*, 2017, **19**, 13970–13977.
- 12 T. Higashino, K. Sugiura, Y. Tsuji, S. Nimura, S. Ito and H. Imahori, *Chem. Lett.*, 2016, **45**, 1126–1128.
- 13 M. B. Thomas, R. G. W. Jindasa, Y. Hu, B. Schmitz, H. Wang and F. D'Souza, *Can. J. Chem.*, 2018, **96**, 881–889.
- 14 P. Arpaçay, P. Maity, A. M. El-Zohry, A. Meindl, S. Akca, S. Plunkett, M. O. Senge, W. J. Blau and O. F. Mohammed, *J. Phys. Chem. C*, 2019, **123**, 14283–14291.
- 15 P. Rathi, Ekta, S. Kumar, D. Banerjee, V. R. Soma and M. Sankar, *Dalt. Trans.*, 2020, **49**, 3198–3208.
- 16 M. O. Senge, M. Fazekas, E. G. A. Notaras, W. J. Blau, M. Zawadzka, O. B. Locos and E. M. N. Mhuircheartaigh, *Adv. Mater.*, 2007, **19**, 2737–2774.
- 17 N. Zarrabi and P. K. Poddutoori, *Coord. Chem. Rev.*, 2021, **429**, in press.
- 18 P. K. Poddutoori, B. J. Bayard, N. Holzer, S. Seetharaman, N. Zarrabi, N. Weidner, P. A. Karr and F. D'Souza, *Inorg. Chem.*, 2021, **60**, 17952–17965.
- 19 P. K. Poddutoori, A. Dion, S. Yang, M. Pilkington, J. D. Wallis and A. Van Der Est, *J. Porphyr. Phthalocyanines*, 2010, **14**, 178–187.
- 20 P. K. Poddutoori, G. N. Lim, M. Pilkington, F. D'Souza and A. Van Der Est, *Inorg. Chem.*, 2016, **55**, 11383–11395.
- 21 N. Zarrabi, B. J. Bayard, S. Seetharaman, N. Holzer, P. Karr, S. Ciuti, A. Barbon, M. Di Valentin, A. Van Der Est, F. D'Souza and P. K. Poddutoori, *Phys. Chem. Chem. Phys.*, 2021, **23**, 960–970.
- 22 S. I. Tsunami, K. Tanaka, J. Matsumoto, T. Shiragami and M. Yasuda, *Bull. Chem. Soc. Jpn.*, 2008, **81**, 583–589.
- 23 T. Shiragami, J. Matsumoto, H. Inoue and M. Yasuda, *J. Photochem. Photobiol. C Photochem. Rev.*, 2005, **6**, 227–248.
- 24 Y. H. Liu, M. F. Bénassy, S. Chojnacki, F. D'Souza, T. Barbour, W. J. Belcher, P. J. Brothers and K. M. Kadish, *Inorg. Chem.*, 1994, **33**, 4480–4484.
- 25 T. Barbour, W. J. Belcher, P. J. Brothers, C. E. F. Rickard and D. C. Ware, *Inorg. Chem.*, 1992, **31**, 746–754.
- 26 H. Inoue, T. Okamoto, Y. Kameo, M. Sumitani, A. Fujiwara, D. Ishibashi and M. Hida, *J. Chem. Soc. Perkin Trans. 1*, 1994, 105–111.
- 27 J. Jiang, K. L. Materna, S. Hedström, K. R. Yang, R. H. Crabtree, V. S. Batista and G. W. Brudvig, *Angew. Chemie - Int. Ed.*, 2017, **56**, 9111–9115.
- 28 T. Shiragami, K. Kubomura, D. Ishibashi and H. Inoue, *J. Am. Chem. Soc.*, 1996, **118**, 6311–6312.
- 29 Y. Andou, T. Shiragami, K. Shima and M. Yasuda, *J. Photochem. Photobiol. A Chem.*, 2002, **147**, 191–197.
- 30 T. Shiragami, Y. Andou, Y. Hamasuna, F. Yamaguchi, K. Shima and M. Yasuda, *Bull. Chem. Soc. Jpn.*, 2002, **75**, 1577–1582.
- 31 M. Ertl, E. Wöß and G. Knör, *Photochem. Photobiol. Sci.*, 2015, **14**, 1826–1830.
- 32 T. Tsukamoto, T. Shimada and S. Takagi, *J. Phys. Chem. A*, 2013, **117**, 13037.
- 33 T. Tsukamoto, T. Shimada and S. Takagi, *RSC Adv.*, 2015, **5**, 8479–8485.
- 34 T. Shiragami, K. Nabeshima, S. Nakashima, J. Matsumoto, S. Takagi, H. Inoue and M. Yasuda, *Bull. Chem. Soc. Jpn.*, 2005, **78**, 2251–2258.
- 35 J. Matsumoto, T. Fuchikawa, Y. Komiya, Y. Fueda, T. Matsumoto, T. Shiragami and M. Yasuda, *Chem. Lett.*, 2005, **34**, 1484–1485.
- 36 A. D. Adleb, F. R. Longo, J. D. Finarelli, J. Goldmacher, J. Assour and L. Korsakoff, *J. Org. Chem.*, 1967, **32**, 476.
- 37 I.-C. Liu, J.-H. Chen, S.-S. Wang and J.-C. Wang, *Polyhedron*, 1996, **15**, 3947–3954.
- 38 P. P. Kumar, G. Premaladha and B. G. Maiya, *J. Chem. Sci.*, 2005, vol. 117, pp. 193–201.
- 39 O. Schalk, H. Brands, T. S. Balaban and A. N. Unterreiner, *J. Phys. Chem. A*, 2008, **112**, 1719–1729.
- 40 N. Zarrabi, S. Seetharaman, S. Chaudhuri, N. Holzer, V. S. Batista, A. Van Der Est, F. D'Souza and P. K. Poddutoori, *J. Am. Chem. Soc.*, 2020, **142**, 10008–10024.
- 41 G. N. Lewis, M. Kasha and B. Gilbert, *J. Am. Chem. Soc.*, 1944, **66**, 2100–2116.